Microstructure and ferroelectricity of $BaTiO_3$ thin films on Si for integrated photonics

Microstructure and ferroelectricity of $BaTiO_3$ thin films on Si for integrated photonics

Kristy J. Kormondy[1 a)], Youri Popoff[2], Marilyne Sousa[2], Felix Eltes[2], Daniele Caimi[2], Marta D. Rossell[3], Manfred Fiebig[4], Patrik Hoffmann[5,6], Chiara Marchiori[2], Michael Reinke[5,6], Morgan Trassin[4], Alexander A. Demkov[1], Jean Fompeyrine[2], and Stefan Abel[2b)]

[1]*Department of Physics, The University of Texas at Austin, Austin, Texas, 78712, USA*
[2]*IBM Research – Zurich, Säumerstrasse 4, 8803 Rüschlikon, Switzerland*
[3]*Electron Microscopy Center, Empa, Swiss Federal Laboratories for Materials Science and Technology, Überlandstrasse 129, 8600 Dübendorf, Switzerland*
[4]*Department of Materials, ETH Zurich, Vladimir-Prelog-Weg 4 10, 8093 Zurich, Switzerland*
[5]*Laboratory for Advanced Materials Processing, Empa, Swiss Federal Laboratories for Materials Science and Technology, Feuerwerkerstrasse 39, 3602 Thun, Switzerland*
[6]*Laboratory for Photonic Materials and Characterization, Ecole Polytechnique Fédérale de Lausanne (EPFL), Station 17, 1015 Lausanne, Switzerland*

Abstract

Significant progress has been made in integrating novel materials into silicon photonic structures in order to extend the functionality of photonic circuits. One of these promising optical materials is $BaTiO_3$ or barium titanate (BTO) that exhibits a very large Pockels coefficient as required for high-speed light modulators. However, all previous demonstrations show a noticable reduction of the Pockels effect in BTO thin films deposited on silicon substrates compared to BTO bulk crystals. Here, we report on the strong dependence of the Pockels effect in BTO thin films on their microstructure, and provide guidelines on how to engineer thin films with strong electro-optic response. We employ several deposition methods such as molecular beam epitaxy and chemical vapor deposition to realize BTO thin films with different morphology and crystalline structure. While a linear electro-optic response is present even in porous, polycrystalline BTO thin films with an effective Pockels coefficient r_{eff} = 6 pm/V, it is maximized for dense, tetragonal, epitaxial BTO films (r_{eff} = 140 pm/V). By identifying the key structural predictors of electro-optic response in BTO/Si, we provide a roadmap to fully exploit the linear electro-optic effect in novel hybrid oxide/semiconductor nanophotonic devices.

[a)] kkormond@utexas.edu
[b)] sab@zurich.ibm.com

I. Introduction

For decades, increasing the efficiency and performance of information processing units has been mainly driven by reducing the size of transistors. However, since the scaling law approaches a natural limit, novel concepts such as the introduction of high-mobility materials as transistor channels or optical links for intra-chip communications have more recently been actively investigated. Indeed, silicon photonics offers low-cost fabrication of high-bandwidth and low-power data transmission techniques beyond what is offered by ordinary electrical connections. [1–5] The technology has been boosted by the development of novel components including silicon passives and germanium detectors, but it still lacks some essential device types such as high-performing optical modulators. Since these components have been mastered in bulk telecommunication applications by the usage of materials with strong electro-optical properties such as lithium niobate,[6] a concerted effort has emerged to integrate similar materials into silicon photonic structures, where the refractive index index n can be expressed in terms of the static external electric field E,[7]

$$n(E) = n_0 - \frac{1}{2} n_0^3 r E, \quad (1)$$

where n_0 is the zero-field value of the refractive index and r is the Pockels coefficient. In particular, the recent integration of barium titanate ($BaTiO_3$) on silicon with large Pockels coefficients [8–11] opens an exciting opportunity for designing and realizing high-speed modulators, and novel device types such as non-volatile optical memories. The latter elements would be of great interest as synaptic elements for optical neural networks.[12]

Despite the recent integration success, the linear electro-optic effect in $BaTiO_3$ (BTO) thin films determined in previous experiments clearly shows deteriorated properties compared to bulk BTO crystals.[8-11] From a materials perspective, understanding the mechanism of this degradation opens exciting opportunities to further engineer and tailor the Pockels coefficients in thin films. We have developed and described in detail a characterization technique which allows us to determine the main tensorial properties of the Pockels effect and to demonstrate BTO ferroelectric switching by means of optical measurements.[8] We have formulated the systematic design rules to tailor deposition parameters and obtain high quality crystalline BTO layers on Si substrates.[13]

In this paper, we demonstrate experimentally how the crystalline quality and film morphology of the active material impacts the magnitude of the Pockels effect. To compare and contrast layers of widely varied properties, we deposited ~100 nm thin BTO films on silicon substrates using several different deposition methods. By analysing the structural and electro-optic characteristics of the layers, we identified key structural predictors of a large Pockels coefficient. In particular, reducing the porosity and increasing the crystalline grain size are the key contributors to maximizing the electro-optic response. Our study outlines the path for material scientists to design highly efficient, novel hybrid silicon photonic devices based on nanoscale oxides integrated on silicon.

II. Methods

Sample preparation

In order to realize different layer properties, we deposited BTO thin films via molecular beam epitaxy (MBE), pulsed laser deposition (PLD), chemical vapor deposition (CVD), and radio-frequency sputtering (RF sputtering). Except when explicitly mentioned, we used a 4-nm-thin $SrTiO_3$ (STO) seed layer grown epitaxially by MBE on highly-resistive (>20,000

Ω·cm) double-side-polished Si (001) wafers for all successive BTO deposition. Details of the STO deposition can be found elsewhere.[14]

Subsequently, BTO was fabricated by MBE (MBE-BTO) in a layer-by-layer deposition process. Therefore, layers of titanium and barium were iteratively deposited in oxygen atmosphere ($p \sim 10^{-5}$ mbar) keeping the substrate at ~600°C. Details of the deposition process are described in Ref. [8]. The PLD thin films (PLD-BTO) were grown at a substrate temperature of 690° C under an oxygen pressure of 0.15 mbar using an excimer KrF laser. The laser repetition rate was set to 2Hz and the fluence at 1.2 Jcm^{-2}. For CVD deposition of BTO the heated substrate (400°C) was exposed to barium isopropyl cyclopentadienyl, titanium isopropoxide and water as reactive precursors in a high vacuum (10^{-6} mbar) environment; comparable to the process described in Ref. [15]. Two additional samples of BTO were prepared by RF sputtering. The first utilized an 8-nm-BTO/4-nm-STO/Si pseudosubstrate prepared by MBE as discussed above, while the second was sputtered directly on Si with no buffer layer using the same parameters as described in Ref. [13]. After the sputter deposition at 500°C, the samples were annealed in oxygen at 650°C for 20 minutes to ensure full crystallization.

Structural characterization

For each of the samples, we extracted the lattice parameters for the BTO film via both out-of-plane and grazing incidence in-plane X-ray diffraction (XRD) measurements using a Bruker AXS D8 Discover. Out-of-plane and in-plane scans are aligned to Si (004) and (220) peaks, respectively. Atomic force microscopy analysis was performed using a Veeco Dimension V. The refractive index, thickness, and porosity of the BTO films have been characterized by spectroscopic ellipsometry using a Variable Angle Spectroscopic Ellipsometer VASE® from J.A. Woollam Co. Data have been acquired for wavelengths between 300 nm and 1200 nm at 3 angles of incidence (65, 70 and 75°).

Cross sectioning and lamella preparation were carried out by means of a FEI Helios Nanolab 450S focused ion beam. Bright-field and medium-angle annular dark field (MAADF) scanning transmission electron microscopy (STEM) measurements were performed using a double spherical aberration-corrected JEOL JEM-ARM200F microscope operated at 200 kV with a probe convergence semiangle set to 25.3 mrad. The annular semi-detection range of the annular dark-field detector was calibrated at 40-160 mrad for the MAADF images. For the bright-field images, the outer semi-detection range of the bright-field detector was set to 45 mrad.

Electro-optic characterization

We determined the Pockels coefficients by analyzing the change of the polarization of a laser beam transmitted through the BTO film while applying an electric field. In order to generate such a field, pairs of 300-nm-thick tungsten electrodes with the electrode gap d = 5 μm were defined by optical lithography and SF_6/N_2 reactive ion etching. In order to assess the tensorial nature of the Pockels effect, we varied the angle θ_E between the electric field and the BTO crystalline axis by fabricating differently oriented electrode pairs, as defined in Figure 1 (a).

The electro-optic characterization follows the principle illustrated in Figure 1(b)-(c) using the Sénarmont set up described in detail elsewhere.[8] A linearly polarized *New Focus* diode laser model 6262 with wavelength 1550 nm focused to a spot size of ~30 μm full-width at half-maximum was first aligned to the electrode gap. A half-wave plate was used to set the incident polarization. Due to the birefringence of BTO, the sample introduces a phase shift

between orthogonal polarization components of the incident light. This phase shift is compensated by a quarter-wave plate (QWP), whose orientation is determined by iteratively rotating the QWP and a successive Glan-laser prism to minimize the transmitted power. After this alignment process, the light after the QWP is linearly polarized. In that configuration, a change of the birefringence in the BTO layer results in a rotation of the polarization after the QWP by an angle δ with respect to the zero-field state.

For increased sensitivity, a lock-in amplifier system was used to isolate the rotation δ induced by a sinusoidal AC field modulated at frequency f = 17.3 kHz. Typical values of the peak-to-peak AC voltage $V_{PP} \sim 3$ V were much smaller than the typical voltage used to align ferroelectric domains $V_{DC} \sim 20$ V. Since in the lock-in configuration only the rotation δ corresponding to the AC modulation is measured, we introduce a field-normalized rotation, $\delta' = \delta / E_{AC}$, where the root mean square AC field was defined as $E_{AC} = \mathrm{V}_{PP} / (2\sqrt{2}d)$ and δ is the rotation defined in Figure 1. The static offset field applied to align ferroelectric domains was defined as $E_{off}=V_{DC}/d$, where d is the gap between electrodes. While the magnitude of this offset field does not enter directly into the definition of the Pockels coefficient, it does influence the fraction of poled domains v. In the presence of polarization-reversed domains as in an un-poled film, a reduced response could be measured due to cancellation of contributions from antiparallel domains, leading to underestimated Pockels coefficients.[17] For this reason, Pockels coefficients reported here are for poled films, corresponding to $v = 1$ at at $\theta_E \sim 45°$ and $v = 0.5$ at at $\theta_E \sim 90°$ as justified in the following sections.

The effective electro-optic coefficient can then be defined as follows,

$$r_{eff} = \Gamma\lambda / (v \times E_{AC} \times \pi \times n_{BTO}^3 \times t), \quad (2)$$

adapted from Ref. [16], where $\Gamma = 2\delta$ is the induced phase shift between orthogonal polarization components, λ = 1550 nm is the wavelength of the transmitted light, v is the net fraction of poled BTO domains, E_{AC} is the measuring field defined above, n_{BTO} is the refractive index of the film, and t is the thickness of the BTO layer. As described in detail elsewhere,[8] the rotation of polarization δ depends strongly on the orientation of the electric field. To capture this dependence and fully describe the Pockels effect, we report both the effective Pockels coefficient r_{eff} and the c-axis Pockels coefficient r_c for each sample. Specifically, we extract r_{eff} from measurements at $\theta_E \sim 45°$ assuming $v = 1$ and r_c from measurements at $\theta_E \sim 90°$ assuming $v = 0.5$.[8] Full dependence of these coefficients on the Pockels tensor elements are discussed in Refs. [8] and [17]. In order to extract Pockels tensor elements in addition to these effective values, numerical simulations based on the Pockels tensor and domain structure were carried out to best approximate δ for all measured electrode angles θ_E.

To accurately represent error bars, several known sources of error, including stability over time, position of the laser within the gap, and angle of incidence, were analyzed: Less than 4% uncertainty originates from experimental error sources. In addition, data was recorded for six sets of similar electrodes with $\theta_E \sim 45°$ for each sample in order to account for pad-to-pad variations originating from materials inhomogeneity. The combined errors are reported later in the manuscript.

III. Results

Structural Characterization

The strong Pockels effect in BTO originates from the peculiarity of the Ti-O bond that results in a combination of a non-centrosymmetric crystal lattice of the tetragonal phase and an anharmonic potential.[18] Therefore, defects that break the periodicity of the lattice and thus

affect long wave length phonons or that influence the crystalline symmetry are expected to diminish the electro-optic response. Examples of the impact of defects on the structural and functional properties of BTO are the stabilization of BTO in the cubic phase for polycrystalline layers with nanometer-sized grains,[13] strain enhancement of the ferroelectric polarization,[19] and relaxor behavior under stoichiometry deviation.[20] Hence, in the following we first discuss in detail the films' morphology and crystalline structure, before analyzing the electro-optic results and correlating both the structural and the functional features.

We determined the porosity and the thickness of the BTO layers by simulating the spectroscopic ellipsometry data with a Bruggeman effective medium approximation model. In this model, we assume the films to consist of a BTO matrix, having the refractive index of bulk BTO along its ordinary axis [21] and a fraction of spherical voids, having the refractive index of air (1.0). The porosity is quantified as the volume fraction p of the voids. In order to reduce the number of fit parameters we neglect the dependence of the refractive index of the BTO matrix on other structural parameters such as grain boundaries, stoichiometry, strain, and crystallographic orientation. This simplification allows us to consistently evaluate the porosity and thickness for all five samples (Table 1). The BTO film thickness extracted from the spectroscopic ellipsometry model and compared with the MAADF-STEM images (Figure 2(a)-(d)) only show slight deviations of <5%. To account for this difference, we determined the uncertainty of p by intentionally varying the thickness of the BTO layer by ±5% around the value initially determined by spectroscopic ellipsometry (Table 1). We could qualitatively verify the large difference in porosity between the films as determined by spectroscopic ellipsometry with our bright-field-STEM analysis, where pores are clearly visible as areas of decreased density (Figure 2 and Supplementary Figure S1). The different surface roughness among the samples is also in agreement with the varying porosity. In particular, the atomic force microscopy of the dense MBE-BTO layer (p = 3%) shows a low root mean square roughness of only ~0.5 nm (Supplementary Figure S2).

With an epitaxial STO buffer layer, the epitaxial relationship of BTO to the Si substrate could be preserved even as an amorphous SiO_x interfacial layer was formed during deposition or post-anneal (Figure 2), in agreement with previous studies.[8,13,22] However, an STO buffer layer might not always prevent the formation of some randomly oriented domains.[13] Indeed, we observe a transition from epitaxial to polycrystalline orientation in the RF sputtered BTO film (Figure 2(c), dashed line). As expected, the film sputtered directly on Si without any buffer layer is fully polycrystalline.[13]

In MAADF-STEM images (Figure 2), the contrast is sensitive to diffraction effects. Accordingly, the crystal lattice of bright grains is oriented along the electron beam, and homogenous brightness indicates homogenous crystalline orientation. Additional contrast modulation, as in Figure 2(a), originates from projecting a 3D domain structure of multiple grains into a 2D image. As a guide to the eye, we highlighted several grains per image in Figure 2. We estimated the grain size by calculating the equivalent disc radius *edr* via $edr = \sqrt{A/\pi}$ (Table 1) where A corresponds to the area of the highlighted grains. While columnar grains with *edr* >20 nm were observed for BTO deposited by MBE and PLD (Figure 2(a) and (b)), smaller grains of *edr* < 15 nm were observed for BTO deposited by CVD and RF sputtering (Figure 2(c) and (d), Table 1).

XRD was employed to quantify tetragonality, a signature of symmetry breaking, of the BTO films. In the ferroelectric phase at room temperature, bulk BTO shows a non-centrosymmetric tetragonal *P*4*mm* symmetry with two distinct lattice parameters, a and c. The tetragonal distortion for bulk crystals is $\gamma = c/a - 1 = 1\%$.[23] Previous studies of MBE-grown

BTO films deposited on STO-buffered Si have shown a multi-domain structure: While thin films are single-domain with the long *c*-axis oriented perpendicular to the interface, a transition occurs for thicker films,[13,22] with a mixture of domains with the *c*-axis oriented perpendicular (along (001)) and parallel to the surface (along (100)/(010)).

Using this "mixed model" of the domain structure (Figure 3(a)) we determined both the *a* and *c* lattice parameters from the XRD data. Therefore, we fit each pair of out-of-plane and in-plane XRD scans simultaneously as the sum of three Voigt functions with shared peak parameters: Two components correspond to the (001)-oriented and (100)/(010)-oriented domains of BTO, with a third component corresponding to cubic STO. The STO component is only applied in samples with STO buffer layer. Figure 3 (b) and (c) illustrate fits to the BTO (002) and (200)/(020) peak of samples deposited by MBE (MBE-BTO) and CVD (CVD-BTO), respectively, with corresponding bulk lattice positions indicated by vertical dashed lines. The tetragonality of the CVD-BTO film is significantly reduced compared to the MBE-BTO film. Lattice parameters and tetragonal distortion γ for all samples are summarized in Table 2. The XRD analysis also confirms the epitaxial relationship between BTO and Si in all samples (Supplementary Figure S3(a)). Only sputtered BTO layers show (110) reflections, indicating a small fraction of polycrystalline domains if a STO seed layer is used and a fully polycrystalline film if no STO layer was deposited. The analysis of the misorientation of crystalline domains assessed via rocking curve measurements of the BTO (002) reflection does not show strong differences among the films, as it is essentially determined by the mosaicity of the underlying STO layer. The rocking curve full-width at half maximum for all samples is within a similar range of 1.2° to 2.1° (Supplementary Figure S3(b)), where the lower and upper bounds correspond to films deposited by PLD and MBE, respectively.

Observing a variation of film density, crystallinity, surface roughness, texture (grain orientation and size), and tetragonality among differently fabricated samples is consistent with observations that film microstructure varies with deposition method,[24] temperature and growth rate [25–27], post-deposition treatments,[28] strain,[29] and stoichiometry.[30] The variation in the BTO films discussed here cannot be used to generally evaluate the different deposition techniques, as none of the deposition has been thoroughly optimized. In this current study, we instead leverage the range of crystalline quality to determine the predictors of electro-optic response.

Electro-optic Characterization

We provide effective Pockels coefficients r_{eff} and the *c*-axis coefficient r_{c} for all samples in Table 3 according to Eq. (2) for comparison with the literature values and for evaluating device applications. Due to the random domain orientation, we can only extract r_{eff} but no individual tensor elements for the fully polycrystalline film. The Pockels coefficients strongly vary among the different samples (Table 3), which is for example directly visible in the comparison of the electro-optic response between MBE-BTO and CVD-BTO (Figure 4).

The dependence of δ' on the orientation angle θ_{E} of in-plane electric field matches our simulations as shown in the examples for MBE-BTO and CVD-BTO (Figure 4). Data for all films are available in Supplementary Figure S4. Following the procedure described in the Supplementary Text, the polarization for light transmitted through a sample can be simulated based on the Pockels tensor for the space group *P*4*mm*, taking thickness values from ellipsometry and assuming bulk values for the refractive indices and birefringence. Because domains with the *c*-axis oriented out-of-plane of the film do not contribute to changes in transmission in our measurement geometry, we assume only in-plane 90° domains for our model in order to report a lower bound for the Pockels coefficients. By simulating the response of the samples for the specific measurement geometry used in our experiments, we extracted

the best fit Pockels tensor elements r_{42} and r_{33} for each BTO sample (Table 3). Because our geometry does not permit independent measurement of r_{33} and r_{13}, we assume the bulk ratio of $r_{33} = 10 \times r_{13}$.[33]

For the determination of the Pockels tensor elements, we also need to take into account the overall ferroelectric domain structure. We evaluate the hysteresis by measuring δ' as a function of the offset field E_{off} for a fixed value $\theta_E \sim 45°$, where δ' and hence the resolution of the experiment is maximized (Figure 5, and Supplementary Figure S5).[8] As described previously,[8] on the macroscopic scale of our gap size, δ' is generally zero for the as-deposited film, reaches a finite remanence value $\delta'_r = \delta'(0)$ after poling with sufficiently large electric fields, and saturates at a maximum rotation of δ_S'. These values are indicated in Figure 5, and Supplementary Figure S5. We can then calculate the remanence ratio or "squareness" factor δ'_r / δ'_s, where a ratio of 1 corresponds to a perfectly square loop, and E_c is the coercive field for each sample (Table 4).

The ferroelectric nature of the films largely varies, ranging from wide hysteresis and large remanence ratio in MBE-BTO to slim hysteresis and reduced remanence in CVD-BTO. Materials with finite remanence can be used for bistable optical switching,[34] while non-memory materials can be used over a broad continuous tuning range.[35] Due to the low leakage current in the μA range even at high voltages of 35V (Supplementary Table S1), the tuning applications can be extremely energy efficient.[10] In principle, the variety of properties render the films applicable for a broad range of application, such as low dielectric loss capacitors or ferroelectric storage.[36]

IV. Discussion

Our results show a strong correlation between the structural and electro-optic properties in BTO thin films. In particular, the consistent reduction of the effective Pockels coefficients for increasing porosity (Figure 6(a)) identifies the density of BTO as a key parameter for obtaining a large electro-optic response. In the following, we discuss the physical origin of this correlation.

Electric Field Distribution

First, we consider the impact of porosity on the electric field distribution in the BTO film. In our derivation of the electro-optic response as a function of the Pockels coefficient (Eq.(2)) we assume the voltage to drop homogenously along the BTO layer. However, due to the low permittivity of the voids compared to the BTO matrix ($\varepsilon_{BTO} >> \varepsilon_{air} = 1$), the electric field distribution might be significantly influenced in porous films. Since we cannot perform capacitance-voltage profiling on the exact samples in this study because of the highly-resistive silicon substrate, we assume the permittivity ε_{BTO} to range from 50 to 660 as reported for thin BTO films on Si.[22,27] A reduction of the effective electric field within the BTO matrix for larger porosities would indeed result in a strong reduction of the electro-optic response for porous films even though the Pockels coefficient of the matrix might not have changed.

From this point of view, the values of the Pockels coefficients estimated earlier (Table 3) have to be considered as the average Pockels coefficients of the porous films, rather than the actual Pockels coefficient of the BTO crystal. Because the electric field is in the denominator of Eq. (2), a porosity correction factor $c_P = E / E_{BTO}$, defined as the ratio between the electric field in a pore-free BTO crystal (E) and the average electric field in the actual matrix of the porous BTO layer (E_{BTO}), can be used to provide a sense of how the Pockels coefficients would scale with porosity.

An electro-static finite elements study has been carried out for different pore geometries. Cylindrically shaped tubes through the material represent the geometry closest to the pores seen in Figure 2. For this geometry, even when assuming the largest experimentally observed porosity (20%) and relative permittivity of $\varepsilon_{BTO} = 660$, the correction factor remains rather moderate ($c_P \sim 1.15$) (Supplementary Figure S6). In contrast to circular pores, fissures in the material would lead to a correction factor between one and two orders of magnitude higher for the same porosity (Supplementary Figure S6). While this analysis shows the importance of obtaining crack-free layers for electro-optic applications, on the basis of TEM and AFM analysis (Figure 2 and Supplementary Figure S2) we preclude fissures as the origin of the reduction of the Pockels effect in our films. The reduction of the electric field in the BTO matrix can thus not be the main origin for the experimentally observed large differences of the electro-optic response between the layers ($r_{eff,max}/r_{eff,miin} \sim 20$). This suggests that the Pockels effect of the BTO matrix has to significantly vary among the films in order to account for our observations of a strongly varying electro-optic response.

Defects in BTO

Next, we consider factors which could impact the electro-optic response of BTO itself. Because the linear electro-optic response originates from the anharmonic nature of the Ti-O bond and the loss of the inversion symmetry in the tetragonal phase (phonon condensation), defects which affect phonons (breaking the periodicity of the lattice, eg. finite size) [37] or restore centrosymmetric structure (eg. antiphase boundaries) [29,38] are expected to diminish the electro-optic response. This is consistent with Figure 6(a), considering pores as defects in the crystal.

In addition to the change in magnitude, it has been already reported that defects such as pores and grain boundaries can stabilize the cubic centrosymmetric phase of BTO, which shows no Pockels effect.[29,39] The reduction of the Pockels effect when increasing the porosity could further be associated to a reduced tetragonality. This hypothesis is verified by comparing the anisotropy of the electro-optic response, defined as the ratio of the Pockels tensor elements r_{42}/r_{33}. In bulk single-crystal BTO, this anisotropy ratio is larger than ~10.[33] We observe in our samples that loss of anisotropy correlates with loss of tetragonal distortion γ (Figure 6(b)). Besides being influenced by porosity, a reduced anisotropy could result also from the influence of strain on the electro-optic tensor.[33]

These two effects, microstructure and symmetry, are in general coupled, as in the case of polycrystalline films containing a higher fraction of cubic BTO.[29] In Figure 6(a)-(b), the reduction in the magnitude and anisotropy of the Pockels tensor for cubic, porous, and polycrystalline films indicates a strong dependence of the electro-optic response on crystalline quality. In particular, high tetragonality and minimal porosity in BTO thin films is essential to achieve bulk-like electro-optic performance.

Memory

Although all films investigated in our study show ferroelectric functionality, strong variations in the remnant polarization response are observed (Figure 5). For the in-plane electrode geometry, low leakage current is needed to prevent film depolarization.[40] In previous studies, functional properties of BTO such as the spontaneous polarization [38] and second harmonic generation [41] improve significantly after poling in fields ~300 kV/cm.[38] Similarly, δ' generally reaches a finite remanence value δ'_r after poling in sufficiently large electric field.[8] In contrast, δ' exists only in the presence of an electric field for materials such as relaxors, where the behavior depends on polar nano-regions.[35] In our study, remanence

correlates with grain size *edr* (Figure 6(c)), consistent with previous observations of reduced remanence for small-grained ceramics.[39] The physical origin of this reduced remanence can be structural defects in the films, for example present at grain boundaries, which pin ferroelectric domains.[13,32,40,42–43] The strong variations of the remanence show an additional degree of freedom in engineering the electro-optic properties of BTO thin films: While films tuned for large grain sizes could be used for non-volatile memories,[34] small-grained layers might be benifical for devices requiring periodic poling [35] or filtering.[44]

In summary, we have identified several key correlations between the structural and electro-optic properties of BTO thin films on silicon. The reduction of the effective Pockels coefficients, anisotropy, and remanence in BTO films on Si are concluded to result from crystalline defects and distortions originating from pores in the film, loss of tetragonality, and the finite size of BTO grains. While a linear electro-optic response was measured even for porous polycrystalline BTO, the response is higher by one order of magnitude for dense, tetragonal, epitaxial BTO films.

V. Conclusion

In conclusion, we analyzed BTO thin films of thickness ranging from 70 to 100 nm deposited by several different methods (MBE, PLD, RF sputtering, and CVD) on STO-buffered Si (001) to produce an array of samples with varied morphology and structural quality. The effective Pockels coefficient varied from 6 to 140 pm/V and remanence ratio from 0.35 to 0.04 under this structural variation. Indeed, even highly porous, polycrystalline BTO films were found to have a linear electro-optic response. Our study provides a link between structural and electro-optic properties of BTO thin films, and demonstrates clearly the effectiveness of applying materials science to tailor customized properties of oxide thin films. While obtaining dense *and* highly tetragonal films is critical to achieve large Pockels coefficient as for example needed in high-speed BTO/Si photonic modulators, fabricating layers with large grain sizes is the crucial parameter to maximize the memory window as needed for non-volatile optical storage. For further development of BTO-based Si photonic devices, additional practical aspects such as the Curie temperature shift [19,40] should be addressed in future studies, as well as exploring routes including strain engineering and doping to enhance the electro-optic coefficients.

Acknowledgments

This work was supported by the National Science Foundation (IRES-1358111), the Air Force Office of Scientific Research (FA9550-12-10494 and FA9550-14-1-0090) and the European Commission (FP7-ICT-2013-11-619456-SITOGA, H2020-ICT-2015-25-688579 PHRESCO).

References

[1] Reed G T, Mashanovich G, Gardes F Y and Thomson D J 2010 Silicon optical modulators *Nat. Photonics* **4** 518–26

[2] Melikyan A, Alloatti L, Muslija A, Hillerkuss D, Schindler P C, Li J, Palmer R, Korn D, Muehlbrandt S, Van Thourhout D, Chen B, Dinu R, Sommer M, Koos C, Kohl M, Freude W and Leuthold J 2014 High-speed plasmonic phase modulators *Nat. Photonics* **8** 229–33

[3] Benner A F, Ignatowski M, Kash J A, Kuchta D M and Ritter M B 2005 Exploitation of optical interconnects in future server architectures *IBM J. Res. Dev.* **49** 755–75

[4] Heck M J R, Chen H-W, Fang A W, Koch B R, Liang D, Park H, Sysak M N and Bowers J E 2011 Hybrid Silicon Photonics for Optical Interconnects *IEEE J. Sel. Top. Quantum Electron.* **17** 333–46

[5] Gourlay J, Forbes M and Desmulliez M 2001 Optically interconnected electronic chips: a tutorial and review of the technology *Electron. Commun. Eng. J.* **13** 221–32

[6] Wooten E L, Kissa K M, Yi-Yan A, Murphy E J, Lafaw D A, Hallemeier P F, Maack D, Attanasio D V, Fritz D J, McBrien G J and Bossi D E 2000 A review of lithium niobate modulators for fiber-optic communications systems *IEEE J. Sel. Top. Quantum Electron.* **6** 69–82

[7] Saleh B E A and Teich M C 1991 *Fundamentals of Photonics* (New York: Wiley)

[8] Abel S, Stöferle T, Marchiori C, Rossel C, Rossell M D, Erni R, Caimi D, Sousa M, Chelnokov A, Offrein B J and Fompeyrine J 2013 A strong electro-optically active lead-free ferroelectric integrated on silicon *Nat. Commun.* **4** 1671

[9] Xiong C, Pernice W H P, Ngai J H, Reiner J W, Kumah D, Walker F J, Ahn C H and Tang H X 2014 Active Silicon Integrated Nanophotonics: Ferroelectric $BaTiO_3$ Devices *Nano Lett.* **14** 1419–25

[10] Abel S, Stoferle T, Marchiori C, Caimi D, Czornomaz L, Stuckelberger M, Sousa M, Offrein B J and Fompeyrine J 2016 A Hybrid Barium Titanate–Silicon Photonics Platform for Ultraefficient Electro-Optic Tuning *J. Light. Technol.* **34** 1688–93

[11] Kormondy K J, Abel S, Fallegger F, Popoff Y, Ponath P, Posadas A B, Sousa M, Caimi D, Siegwart H, Uccelli E, Czornomaz L, Marchiori C, Fompeyrine J and Demkov A A 2015 Analysis of the Pockels effect in ferroelectric barium titanate thin films on Si(001) *Microelectron. Eng.* **147** 215–8

[12] Vandoorne K, Mechet P, Van Vaerenbergh T, Fiers M, Morthier G, Verstraeten D, Schrauwen B, Dambre J and Bienstman P 2014 Experimental demonstration of reservoir computing on a silicon photonics chip. *Nat. Commun*. **5** 3541

[13] Abel S, Sousa M, Rossel C, Caimi D, Rossell M D, Erni R, Fompeyrine J and Marchiori C 2013 Controlling tetragonality and crystalline orientation in $BaTiO_3$ nano-layers grown on Si *Nanotechnology* **24** 285701

[14] Marchiori C, Sousa M, Guiller A, Siegwart H, Locquet J-P, Fompeyrine J, Norga G J and Seo J W 2006 Thermal stability of the $SrTiO_3$/(Ba,Sr)O stacks epitaxially grown on Si *Appl. Phys. Lett.* **88** 072913

[15] Reinke M, Kuzminykh Y and Hoffmann P 2015 Combinatorial HV-CVD survey of barium triisopropyl cyclopentadienyl and titanium tetraisopropoxide for the deposition of BaTiO3 *Phys. status solidi* **212** 1556–62

[16] Reitze D H, Haton E, Ramesh R, Etemad S, Leaird D E, Sands T, Karim Z and Tanguay A R 1993 Electro-optic properties of single crystalline ferroelectric thin films *Appl. Phys. Lett.* **63** 596–8

[17] Abel S, Caimi D, Sousa M, Stöferle T, Rossel C, Marchiori C, Chelnokov A and Fompeyrine J 2012 Electro-optical properties of barium titanate films epitaxially grown on silicon *SPIE OPTO* **8263** 82630Y

[18] Veithen M, Gonze X and Ghosez P 2005 Nonlinear optical susceptibilities, Raman efficiencies, and electro-optic tensors from first-principles density functional perturbation theory *Phys. Rev. B* **71** 125107
[19] Choi K J, Biegalski M, Li Y L, Sharan A, Schubert J, Uecker R, Reiche P, Chen Y B, Pan X Q, Gopalan V, Chen L-Q, Schlom D G and Eom C B 2004 Enhancement of ferroelectricity in strained $BaTiO_3$ thin films. *Science* **306** 1005–9
[20] Ravez J, Broustera C and Simon A 1999 Lead-free ferroelectric relaxor ceramics in the $BaTiO_3$-$BaZrO_3$-$CaTiO_3$ system *J. Mater. Chem.* **9** 1609–13
[21] Palik E D 1991 Handbook of optical constants of solids II *Bost. Acad. Press* 1096
[22] Dubourdieu C, Bruley J, Arruda T M, Posadas A, Jordan-Sweet J, Frank M M, Cartier E, Frank D J, Kalinin S V, Demkov A A and Narayanan V 2013 Switching of ferroelectric polarization in epitaxial $BaTiO_3$ films on silicon without a conducting bottom electrode *Nat. Nanotechnol.* **8** 748–54
[23] Jona F and Shirane G 1962 *Ferroelectric crystals* (Pergamon Press)
[24] Michalak D J, Blackwell J M, Torres J M, Sengupta A, Kreno L E, Clarke J S and Pantuso D 2015 Porosity scaling strategies for low-k films *J. Mater. Res.* **30** 3363–85
[25] Ambriz-Vargas F, Velasco-Davalos I, Thomas R and Ruediger A 2016 Nucleation and growth of ultrathin $BaTiO_3$ films on single terminated Nb:$SrTiO_3$ (100) substrates for ferroelectric tunnel junctions *J. Vac. Sci. Technol. B* **34** 02M101
[26] Wills L A, Wessels B W, Richeson D S and Marks T J 1992 Epitaxial growth of $BaTiO_3$ thin films by organometallic chemical vapor deposition *Appl. Phys. Lett.* **60** 41
[27] Ngo T Q, Posadas A B, McDaniel M D, Hu C, Bruley J, Yu E T, Demkov A A and Ekerdt J G 2014 Epitaxial c-axis oriented $BaTiO_3$ thin films on $SrTiO_3$-buffered Si(001) by atomic layer deposition *Appl. Phys. Lett.* **104** 082910
[28] McDaniel M D, Posadas A, Ngo T Q, Dhamdhere A, Smith D J, Demkov A A and Ekerdt J G 2013 Epitaxial strontium titanate films grown by atomic layer deposition on $SrTiO_3$-buffered Si(001) substrates *J. Vac. Sci. Technol. A* **31** 01A136
[29] Li J Y, Rogan R C, Üstündag E and Bhattacharya K 2005 Domain switching in polycrystalline ferroelectric ceramics *Nat. Mater.* **4** 776–81
[30] Brooks C M, Wilson R B, Schäfer A, Mundy J A, Holtz M E, Muller D A, Schubert J, Cahill D G and Schlom D G 2015 Tuning thermal conductivity in homoepitaxial $SrTiO_3$ films via defects *Appl. Phys. Lett.* **107** 051902
[31] Park J W, Baek S H, Bark C W, Biegalski M D and Eom C B 2009 Quasi-single-crystal (001) $SrTiO_3$ templates on Si *Appl. Phys. Lett.* **95** 061902
[32] Zhang L, Wang Y and Engel-Herbert R 2016 Improving the structural quality and electrical resistance of $SrTiO_3$ thin films on Si (001) via a two-step anneal *J. Appl. Phys.* **119** 045301
[33] Zgonik M, Bernasconi P, Duelli M, Schlesser R, Günter P, Garrett M H, Rytz D, Zhu Y and Wu X 1994 Dielectric, elastic, piezoelectric, electro-optic, and elasto-optic tensors of BaTiO 3 crystals *Phys. Rev. B* **50** 5941–9
[34] Borrelli N F and Layton M M 1969 Electrooptic properties of transparent ferroelectric glass—Ceramic systems *IEEE Trans. Electron Devices* **16** 511–4
[35] Haertling G H 1999 Ferroelectric Ceramics: History and Technology *J. Am. Ceram. Soc.* **82** 797–818
[36] Damjanovic D 2006 Hysteresis in piezoelectric and ferroelectric materials *Sci. Hysteresis* **3** 337–465
[37] Merz W J 1956 Switching Time in Ferroelectric $BaTiO_3$ and Its Dependence on Crystal Thickness *J. Appl. Phys.* **27** 938
[38] Lu H A, Wills L A and Wessels B W 1994 Electrical properties and poling of $BaTiO_3$ thin films *Appl. Phys. Lett.* **64** 2973

[39] Okazaki K and Nagata K 1973 Effects of Grain Size and Porosity on Electrical and Optical Properties of PLZT Ceramics *J. Am. Ceram. Soc.* **56** 82–6

[40] Niu G, Yin S, Saint-Girons G, Gautier B, Lecoeur P, Pillard V, Hollinger G and Vilquin B 2011 Epitaxy of $BaTiO_3$ thin film on Si(001) using a $SrTiO_3$ buffer layer for non-volatile memory application *Microelectron. Eng.* **88** 1232–5

[41] Lu H A, Wills L A, Wessels B W, Lin W P, Zhang T G, Wong G K, Neumayer D A and Marks T J 1993 Second-harmonic generation of poled $BaTiO_3$ thin films *Appl. Phys. Lett.* **62** 1314

[42] Ortega N, Kumar A, Scott J F, Chrisey D B, Tomazawa M, Kumari S, Diestra D G B and Katiyar R S 2012 Relaxor-ferroelectric superlattices: high energy density capacitors *J. Phys. Condens. Matter* **24** 445901

[43] Samara G A 2003 The relaxational properties of compositionally disordered ABO_3 perovskites *J. Phys. Condens. Matter* **15** R367–411

[44] Haertling G H 1987 PLZT electrooptic materials and applications—a review *Ferroelectrics* **75** 25–55

Tables

Table 1: Summary of film microstructure parameters. From ellipsometry, we extract the refractive index *n* of the BTO matrix, porosity volume fraction *p* and thickness of the BTO layer *t*. Error bars of porosity correspond to a BTO thickness variation of 5% (details in the text). From STEM, *edr* is the average equivalent disc radius of the grains highlighted in Figure 2.

BTO Method	Buffer Layer	*n*	*p* [%]	*t* [nm]	Texture	*edr* [nm]
MBE	4 nm MBE STO	2.27	3 (±2)	78	Epitaxial	21 (±6)
PLD	4 nm MBE STO	2.18	14 (±3)	97	Epitaxial	21 (±4)
RF Sputter	4 nm MBE STO + 8 nm MBE BTO	2.21	11 (±3)	96	Epitaxial + Polycrystalline	10 (±2)
CVD	4 nm MBE STO	2.13	21 (±1)	70	Epitaxial	14 (±1)
RF Sputter (no buffer)	--	2.12	21 (±3)	102	Polycrystalline	--

Table 2: Results from XRD analysis of *c* and *a* lattice parameters for BTO *P*4*mm* symmetry. Tetragonality $\gamma = c/a - 1$. Error bars correspond to uncertainty of fit parameters.

BTO Method	Peak	*a* / *c* [Å]	γ [(%]
MBE	(002)	3.99 / 4.03	1.0 (±0.1)
PLD	(002)	4.00 / 4.02	0.6 (±0.1)
RF Sputter	(002)	3.99 / 4.05	1.7 (±0.1)
CVD	(002)	4.01 / 4.02	0.3 (±0.3)
RF Sputter (no buffer)	(110)	4.03 / 4.04	0.2 (±0.4)

Table 3: Summary of best-fit Pockels tensor elements r_{42} and r_{33} for each BTO sample. Effective Pockels coefficient r_{eff} and *c*-axis coefficient r_c are calculated according to Eqs. (2). Error bars for r_{42} and r_{42} correspond to a variation of . Error bars for r_{eff} and r_c correspond to pad-to-pad variation determined from multiple measurements of the $\theta_E = 45°$ orientation for each sample.

BTO Method	r_{42} [pm/V]	r_{33} [pm/V]	r_{eff} [pm/V]	r_c [pm/V]
MBE	85 (±0.6)	20 (±0.4)	140 (±18)	20 (±3)
PLD	26 (±0.2)	16 (±0.3)	37 (±27)	14 (±11)
RF Sputter	27 (±0.2)	5.1 (±0.1)	41 (±15)	7 (±3)
CVD	4.5 (±0.1)	6.2 (±0.1)	7 (±4)	5 (±3)
RF Sputter (no buffer)	N/A	N/A	6 (±1)	3 (±1)

Table 4: Summary of parameters related to ferroelectricity from electro-optic measurements, remanence ratio δ'_r / δ'_s and coercive field E_c. Error bars correspond to uncertainty of fit parameters.

BTO Method	δ'_r / δ'_s [%]	E_c [kV/cm]
MBE	35 (±3)	7 (±0.4)
PLD	34 (±2)	18 (±1)
RF Sputter	10 (±5)	4 (±2)
CVD	4 (±4)	2 (±2)
RF Sputter (no buffer)	5 (±4)	4 (±3)

Figures

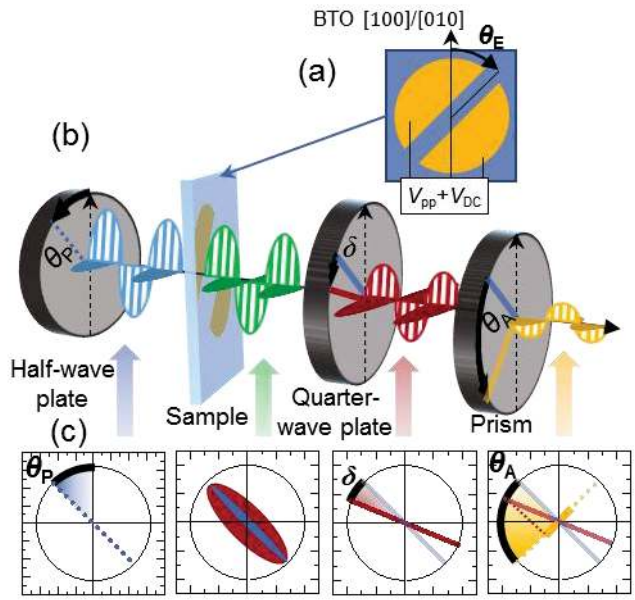

Figure 1: (a) In-plane electrode pairs were patterned with various angles θ_E defined relative to the BTO [100]/[010]/[001] direction. As described in the text, the sinusoidal measuring and static poling voltages V_{pp} + V_{DC} are applied across the electrodes. (b) For electro-optic transmission measurements, a half-wave plate is used to set the incident linear polarization. After passing through the sample, the light becomes elliptically polarized, which is transformed into linearly polarized light after passing a quarter-wave plate. Finally, a Glan-laser prism is used to determine the orientation of the transmitted polarization. (c) Corresponding states of the polarization along the path of the laser beam are visualized as the ellipse traced out by the light's electric field vector with (red) and without (blue) an external electric field. After transmission through the sample and quarter-wave plate, the polarization is rotated by angle δ.

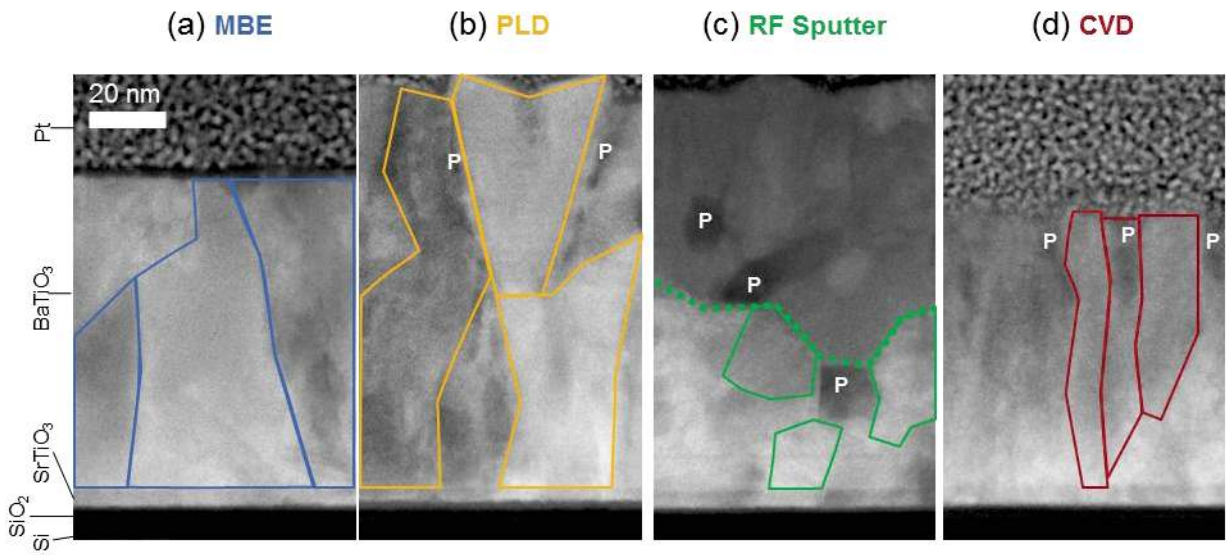

Figure 2: (a) Medium-angle annular dark-field scanning transmission electron microscopy (MAADF-STEM) images of BTO thin films deposited by MBE, (b) PLD, (c) RF sputtering, and (d) CVD. Pores are labelled "P". The boundaries of representative grains are outlined with solid lines. In (c), the boundary between epitaxial and polycrystalline BTO is indicated with dashed line.

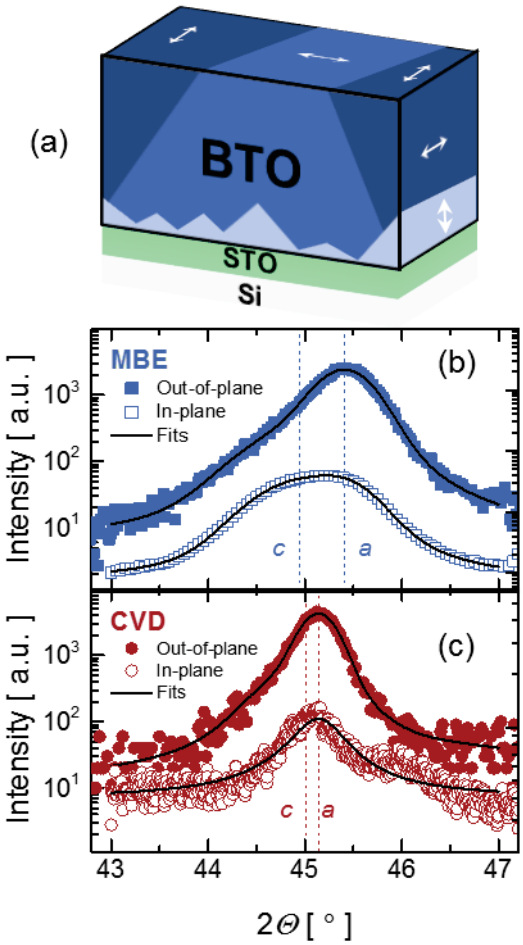

Figure 3 (a) Schematic of 90° domain structure, with the BTO tetragonal axes indicated by white arrows. (b) X-ray diffraction patterns for different measurement configurations for epitaxial BTO deposited by MBE and (c) CVD. A sum of 3 Voigt functions has been fitted to each pair of scans (solid lines), with vertical dashed lines indicating the positions of the peaks corresponding to the BTO *a* and *c* lattice parameters.

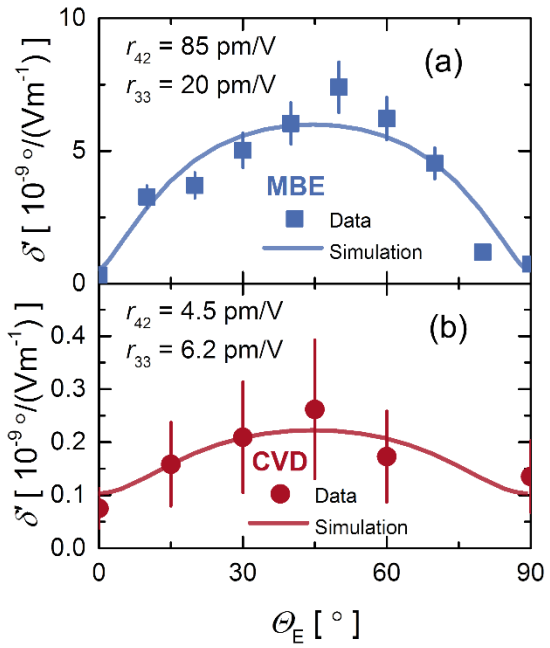

Figure 4: The field-normalized induced rotation δ' was measured (symbols) and simulated (lines) for varied orientation angle θ_E (defined in Figure 1(a)) of in-plane electric field for BTO films deposited by (a) MBE and (b) CVD. Details on error bars can be found in the methods section.

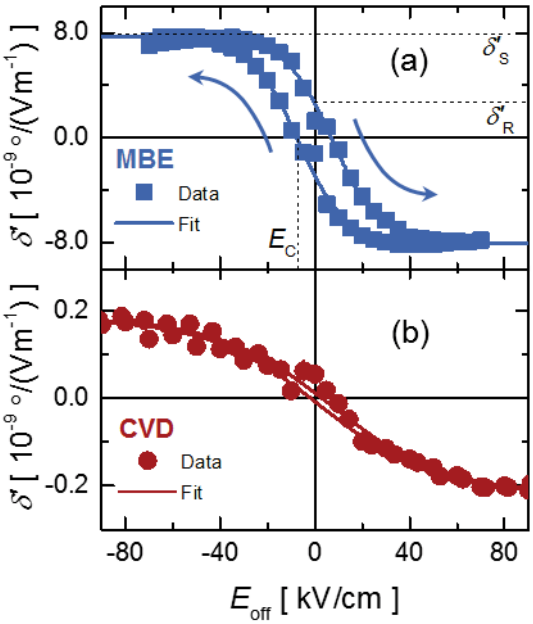

Figure 5: (a) The field-normalized induced rotation δ' measured as a function of a DC offset bias for BTO deposited by MBE and (b) CVD. Sigmoidal fits (solid lines) are utilized to extract saturation and remanent response, δ'_s and δ'_r respectively, as well as the coercive field E_c. Sweep direction is indicated by arrows, with sigmoidal fits to the data described in Supplementary Text.

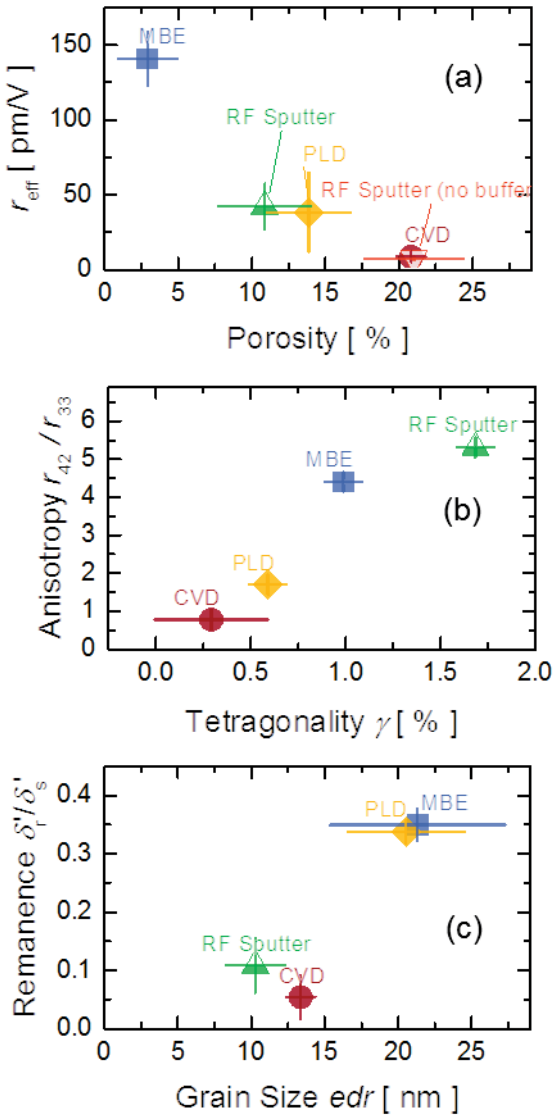

Figure 6: (a) Effective Pockels coefficient r_{eff} vs porosity, (b) anisotropy ratio of Pockels tensor elements r_{42}/r_{33} vs tetragonal distortion γ, where cubic BTO corresponds to $\gamma = 0$, and (c) remanence ratio or squareness factor δ'_r / δ'_s vs. grain size *edr*. Open symbols: polycrystalline, filled symbols: textured/epitaxial, half-filled indicates a mixture.